

Decadal Variability of the Pacific Shallow Overturning Circulation and the Role of Local Wind Forcing

ANTONIETTA CAPOTONDI^{a,b} AND BO QIU^c

^a *Cooperative Institute for Research in Environmental Sciences, University of Colorado Boulder, Boulder, Colorado*

^b *NOAA/Physical Sciences Laboratory, Boulder, Colorado*

^c *Department of Oceanography, University of Hawai'i at Mānoa, Honolulu, Hawaii*

(Manuscript received 29 May 2022, in final form 12 September 2022)

ABSTRACT: The Pacific shallow meridional overturning circulations, known as subtropical cells (STCs), link subduction in the subtropical regions to equatorial upwelling, suggesting the possibility for subtropical winds to influence equatorial sea surface temperatures (SSTs) by altering the STCs' strength. Indeed, STC variability provides the basis for one of the mechanisms proposed to explain the origin of tropical Pacific decadal variability (TPDV). While the relationship between STC strength, as measured by their subsurface transport convergence, and equatorial SST variations is well documented, the location of the wind forcing most influential on STC variability is still being debated. In this study, we use the output of an ocean reanalysis to examine tropical Pacific Ocean surface and subsurface decadal changes during recent decades and relate them to STC variability and surface wind forcing. Our results indicate that the STC interior transport at each latitude is largely controlled by the wind forcing at that latitude rather than induced by remote subtropical wind variations. We also show that the establishment of the anomalous transport at each latitude is associated with the westward propagation of oceanic wind-forced Rossby waves, as part of the ocean adjustment process that also leads to a zonal redistribution of upper-ocean heat content at both interannual and decadal time scales. These results provide guidance for understanding the origin of TPDV by elucidating the underlying dynamics of STC variability and can have practical implications for monitoring STC variability in the tropical Pacific.

SIGNIFICANCE STATEMENT: Slow variations of the surface ocean temperature in the tropical Pacific Ocean have been shown to affect the global climate. Our study aims at better understanding the origin of these temperature anomalies by taking a closer look at the upper ocean circulation variability and its relationship with surface wind forcing. Unlike previous studies, which have related the upper ocean circulation changes to wind variations outside the tropical Pacific, we show here that the variations in upper-ocean circulation are primarily driven by local winds. This result not only clarifies which winds are most important, but also suggests a practical approach for monitoring circulation changes from surface observations.

KEYWORDS: Rossby waves; Ekman pumping; ENSO; Decadal variability; Oceanic variability

1. Introduction

The Pacific Ocean is characterized by pronounced natural variations at decadal time scales with significant impacts on weather and ocean extremes (Wei et al. 2021; Capotondi et al. 2022), trends in surface solar radiation over Northern Hemisphere continents (Augustine and Capotondi 2022), and marine ecosystems (e.g., Mantua et al. 1997; Chavez et al. 2003; Di Lorenzo et al. 2008). These low-frequency variations at time scales longer than approximately 7 years—that is, longer than the dominant time scales of El Niño–Southern Oscillation (ENSO)—have been described in terms of the Pacific decadal oscillation (PDO; Mantua et al. 1997) and the North Pacific Gyre Oscillation (NPGO; Di Lorenzo et al. 2008) in the North Pacific, and in terms of the interdecadal Pacific oscillation (IPO; e.g., Henley et al. 2015) over the entire Pacific basin. Indices of the PDO and NPGO are shown in Fig. 1. Although

PDO and NPGO are identified through empirical orthogonal function (EOF) analysis of monthly SST and sea surface height (SSH) anomalies, respectively, with no temporal filtering applied, they both display low-frequency variations, which tend to be more pronounced in recent decades for the NPGO (Fig. 1).

The spatial pattern of Pacific decadal variability includes a large tropical signature, with anomalies of the opposite sign in the central North and South Pacific relative to the tropics (Power et al. 2021). Although “ENSO-like” (Zhang et al. 1997), the tropical pattern has a broader meridional extent than typical ENSO patterns, and exhibits the largest anomalies in the central Pacific rather than in the eastern Pacific where the more intense ENSO events generally peak (Capotondi et al. 2015, 2020a; Power et al. 2021). Tropical Pacific decadal variability (TPDV) can have global impacts, as exemplified by its influence on the rate of increase of globally averaged surface temperatures (Kosaka and Xie 2013). Oceanic and atmospheric processes involved in TPDV may also control the phase transition of the IPO (Meehl et al. 2016, 2021), affecting decadal variations over the entire basin (Trenberth and Hurrell 1994). Thus, improved understanding of TPDV and its predictability is of paramount importance.

A leading mechanism proposed to explain decadal SST anomalies in the tropical Pacific involves changes in the

^a Denotes content that is immediately available upon publication as open access.

Corresponding author: Antonietta Capotondi, antonietta.capotondi@noaa.gov

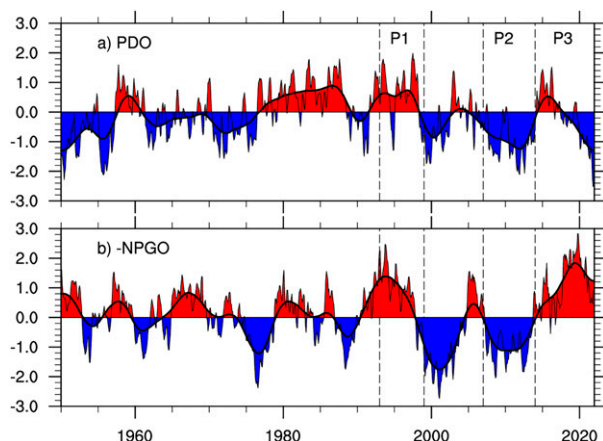


FIG. 1. Time evolution of the (a) Pacific decadal oscillation (PDO) and (b) negative North Pacific Gyre Oscillation (NPGO) indices. The PDO index in (a) is based on the Extended Reconstructed SST, version 5 (ERSSTv5; Huang et al. 2017), and is computed as the leading principal component (PC) of monthly North Pacific (20° – 70° N) SST anomalies (Mantua et al. 1997). The latter are obtained by removing both the climatological annual cycle and the global mean SST anomaly at each grid point. The NPGO index in (b) is obtained as the second PC of SSH anomalies in the northeastern Pacific (180° – 110° W, 25° – 62° N; Di Lorenzo et al. 2008), computed from a blend of ocean model hindcasts and AVISO SSH data. AVISO SSH anomalies are obtained by removing the mean annual cycle over the period 1993–2004, which is the overlapping period between AVISO and the model output. The thin black line in (a) and (b) is a 3-month running average of the indices, and the thick black line shows their 6-yr low-pass filtered version, where the filtering is performed using the approach of Zhang et al. (1997). Vertical dashed lines highlight the three periods considered for some of the analyses. Red shading in (a) and (b) identifies periods characterized by warm conditions in the tropical Pacific, and blue shading corresponds to cooler tropical epochs.

strength of the upper-ocean overturning circulation connecting the subtropical and equatorial regions, known as subtropical cells (STCs). The STCs have traditionally been described in terms of a zonally averaged circulation, with subtropical subduction, equatorward advection of cooler subtropical waters in the pycnocline, equatorial upwelling, and a return poleward flow in the surface Ekman layer. Thus, an increase (decrease) in the strength of this circulation will result in enhanced (reduced) equatorial upwelling, and cooler (warmer) equatorial SSTs. This mechanism, known as the “ $\nu'\bar{T}$ hypothesis” (Kleeman et al. 1999), was proposed as an alternative to the $\bar{\nu}T'$ hypothesis, in which temperature anomalies subducted in the midlatitudes were hypothesized to be advected by the mean circulation to the equatorial thermocline, where they could reach the surface and change the phase of the decadal cycle (Gu and Philander 1997). Since midlatitude temperature anomalies were shown to decay prior to reaching the tropical region (Schneider et al. 1999; Capotondi and Alexander 2001), the scientific community considered the impact of a changing circulation on the generation of equatorial SST anomalies as an alternative mechanism (McCreary and Lu 1994; Solomon et al. 2003). Recent studies have shown, however,

that mean advection of temperature anomalies from the subtropical regions, rather than the midlatitudes, may also contribute to low-frequency variability of equatorial SSTs, especially if the temperature anomalies originate in the Southern Hemisphere (e.g., Imada et al. 2016) and are density-compensated by salinity (i.e., they are “spiciness” anomalies), so that they undergo reduced dissipation (Zeller et al. 2021).

The effectiveness of the $\nu'\bar{T}$ mechanism involving STC variability was demonstrated in several studies using observations (McPhaden and Zhang 2002, 2004), general circulation models of different complexity (e.g., Solomon et al. 2003; Capotondi et al. 2005, hereinafter CADM; Cheng et al. 2007; Lübbecke et al. 2008; Yamanaka et al. 2015; Graffino et al. 2019), and ocean reanalyses (Schott et al. 2007, 2008). In particular, the observational study of McPhaden and Zhang (2002) showed that a decrease in the STC strength in both hemispheres, as estimated from changes in the interior equatorward convergent transport, was concurrent with the tropical Pacific warming that followed the late 1970s PDO phase transition, known as the “1976/77 climate shift” (Fig. 1). A rebound of the overturning circulation was documented toward the end of the 1990s (McPhaden and Zhang 2004), leading to a new cold phase of tropical Pacific decadal variability. This cold period during the first decade of the twenty-first century was considered as a primary driver of the observed slowdown of globally averaged surface temperature trend (Kosaka and Xie 2013) and found to be associated with a profound reorganization of tropical upper-ocean heat content (England et al. 2014). Unlike the 1976/77 climate shift, which was related to a negative-to-positive PDO transition, the 1999/2000 EOF transition was ascribed to a phase change of the second EOF of North Pacific SST anomalies (Bond et al. 2003), a pattern of variability closely related to the NPGO (Di Lorenzo et al. 2008). The NPGO index indeed transitioned from negative (warmer tropical conditions) to positive (cooler tropical conditions) values in the late 1990s, with a brief return to negative values during 2005–07, a behavior similar to that exhibited by the PDO (Fig. 1). However, unlike the PDO, which has remained predominantly negative until 2021, the NPGO index in Fig. 1 shows a distinct transition from positive to negative (i.e., a return to warm tropical conditions) after 2013/14, suggesting a new phase shift in TPDV. To date, however, this recent transition has not been documented from an oceanographic viewpoint. Both PDO and NPGO have been related to the two leading modes of internal atmospheric variability (Di Lorenzo et al. 2022), with the PDO being associated to variability of the Aleutian low, and the NPGO being energized by the North Pacific Oscillation (NPO; Rogers 1981), so that their evolution and phase transitions may partly reflect the stochastic nature of internal atmospheric variations. In addition, as “statistical” modes, their variations may result from the superposition of different dynamical processes, as illustrated for the PDO by Newman et al. (2016). Thus, the evolution and relative phase of PDO and NPGO can be expected to be unrelated.

The STCs are a wind-driven circulation, but the location of the winds that are most influential in changing their strength remains a matter of debate. Given that the subduction branch

of the STCs originates in the subtropics, wind variations in that area have been considered critical for altering the STC strength. Indeed, the idealized numerical model used in the seminal work of McCreary and Lu (1994) indicated that wind variations at the outcrop latitude of the model pycnocline layer ($\sim 18^\circ$) played a key role in the development of equatorial SST anomalies. Subsequent studies with ocean general circulation models forced by anomalous winds in different latitude bands (Nonaka et al. 2002; Lübbecke et al. 2008; Farneti et al. 2014; Graffino et al. 2019) highlighted the importance of wind variations equatorward of about 20° – 25° for altering the strength of the STCs, with equatorial winds alone being unable to significantly affect the circulation in off-equatorial regions (Graffino et al. 2019). These results are consistent with the findings of CADM, which related decadal variations in equatorial upwelling to changes in the strength of off-equatorial trade winds, while equatorial wind anomalies were predominantly associated with ENSO at interannual time scales. CADM also suggested that changes in the transport at a given latitude was accomplished through westward oceanic Rossby wave propagation, a result that highlighted the importance of the local wind forcing at that latitude, in contrast to remote subtropical wind forcing near the outcrop locations, for controlling the STC transport at that latitude. A more precise assessment of the contribution of wind forcing at a given tropical latitude on the decadal ocean changes at that latitude would provide important guidance for better understanding the nature and origin of the winds relevant for TPDV, but no conclusive agreement has yet been reached on the relative role of local versus remote wind forcing.

Thus, this paper intends to revisit this open issue, with three major foci: 1) documenting the surface and subsurface tropical Pacific changes associated with the NPGO transition in 2013/14 in relation to the previous transition in the late 1990s, 2) clarifying the extent to which STC transport variations are related to local wind forcing, and 3) elucidating the relationship between STC variability (usually described in a zonally averaged fashion) and zonal redistribution of heat in the tropical Pacific. After describing the data used (section 2), we examine the observed changes in surface and subsurface conditions across the two NPGO phase transitions (section 3). We then diagnose the variations of the equatorward thermocline transport convergence in the tropical Pacific and show its close connection with equatorial SST anomalies (section 4). These changes in zonally averaged transport are then interpreted in the context of a 1.5-layer shallow-water model to show that they are strongly correlated to the zonal gradient of SSH across the basin and primarily result from westward propagation of oceanic Rossby waves forced by the anomalous Ekman pumping along that same latitude (section 5). We discuss the results in section 6 and conclude in section 7.

2. Data

The primary dataset used for this study is the output of the National Centers for Environmental Prediction (NCEP) Global Ocean Data Assimilation System (GODAS) reanalysis (Behringer and Xue 2004). The model domain extends from

70°S to 65°N with a 1° horizontal resolution, which is meridionally enhanced to $\frac{1}{3}^\circ$ within 10° of the equator. GODAS has 40 vertical layers with a vertical resolution of 10 m in the upper 200 m. GODAS' output includes the surface fields used to force the model, thus allowing to diagnose the impact of the atmospheric wind forcing on the ocean variability. GODAS is used operationally to initialize the NCEP Climate Forecasting System (CFS), so its output is available in quasi real time starting in January 1980. For this study, we consider the period January 1980–December 2020 at a monthly time resolution. GODAS assimilates temperature profiles from moored arrays and Argo floats. Altimeter data are not assimilated, so that they can be used as an independent reference dataset.

To characterize decadal changes in the tropical Pacific we also use other observational datasets. SST data are obtained from the monthly NOAA Optimum Interpolation Sea Surface Temperature (OISST), version 2, at $1^\circ \times 1^\circ$ horizontal resolution from January 1982 to December 2020 (Reynolds et al. 2002), SSH is obtained from AVISO at a 0.25° resolution from January 1993 to December 2019 (<http://www.aviso.oceanobs.com/en/data/products/>), and sea level pressure (SLP) and surface wind vectors are from the NCEP–NCAR reanalysis (Kalnay et al. 1996). The PDO index is downloaded from the NOAA/Physical Sciences Laboratory (NOAA/PSL) website (<https://psl.noaa.gov/pdo/>), based on the NOAA ERSSTv5 dataset (Huang et al. 2017). The index is computed as the leading principal component of monthly SST anomalies north of 20°N . The NPGO index is obtained online (<http://www.o3d.org/npgo/>). The index is defined as the second principal component of SSH over the northeastern Pacific (180° – 110°W , 25° – 62°N) based on the output of a high-resolution simulation (Di Lorenzo et al. 2008) covering the period 1950–2004. After 2004, the index is updated by projecting SSH anomalies from AVISO on the NPGO pattern.

Monthly anomalies of all the fields are obtained by removing the climatological seasonal cycle. To focus on variations at decadal time scales, the GODAS data have been linearly detrended over the total 1980–2020 period prior to the analysis. While some climate fields (e.g., the globally averaged surface temperature) show a nonlinear trend since 1850, with a steeper increase after about 1980, the trend after this date appears to be reasonably linear, thus justifying our choice of linear detrending over the time period covered by GODAS.

3. Surface and subsurface signature of decadal phase transitions

To identify the surface and subsurface changes associated with tropical Pacific decadal phase transitions we consider three periods occurring during different phases of the decadal “cycle” and available across the various datasets: period 1 (P1; 1993–99), period 2 (P2; 2007–13), and period 3 (P3; 2014–20). Each period is 7 years long, to match the duration of the most recent period. Such a duration should be sufficient to average over at least one ENSO cycle (approximately 4–5 years), and reveal the decadal signal, as discussed in McPhaden and Zhang (2004). P1 occurs during warmer tropical Pacific conditions, P2 is part of the period of enhanced

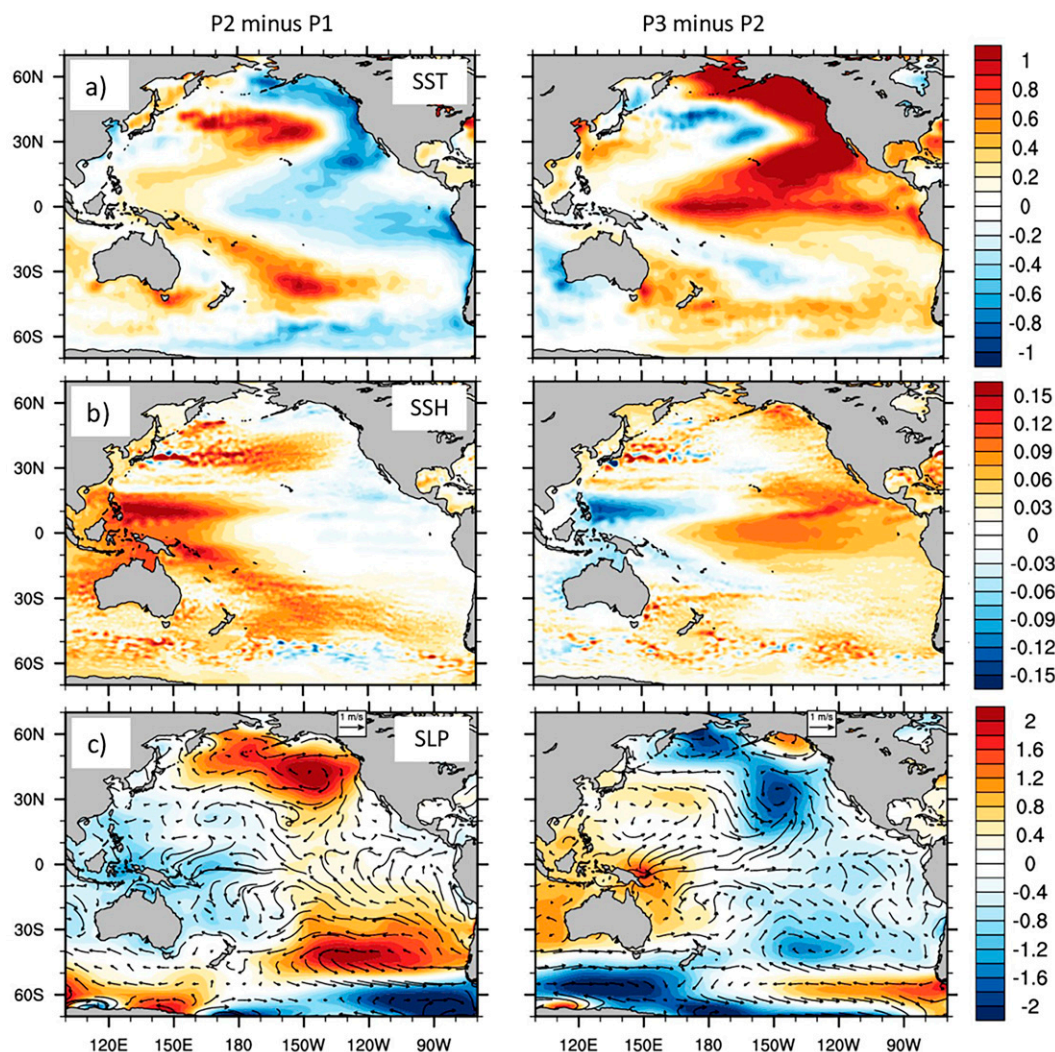


FIG. 2. Basinwide changes associated with TPDV transitions. Differences of (a) SST ($^{\circ}\text{C}$), (b) SSH (m), and (c) SLP (hPa) and vector winds (m s^{-1}) between (left) P2 and P1 and (right) P3 and P2, where P1 is 1993–99, P2 is 2007–13, and P3 is 2014–20. Interannual anomalies have been computed by removing monthly averages over 1993–2020. No detrending is applied to any of the data. SST data are from OISST-V2 (Reynolds et al. 2002), SSH is obtained from AVISO, and the SLP and vector winds are from the NCEP–NCAR reanalysis (Kalnay et al. 1996).

tropical Pacific cooling concurrent with the slowdown of globally averaged surface temperature increase (e.g., Kosaka and Xie 2013; England et al. 2014), and P3 spans the last part of the record, with an expected return to warmer conditions. We start by considering period differences of surface observed quantities (Fig. 2). P2 exhibits cooler SST anomalies in the tropical Pacific relative to P1, with anomalies of the opposite sign in the central-western midlatitudes (30° – 40°) of both hemispheres. The SST anomaly pattern is quasi-symmetric about the equator, and reminiscent of the IPO (Henley et al. 2015). SSH differences show a pronounced zonal asymmetry in the tropical Pacific, characterized by weak negative anomalies (corresponding to a shallower thermocline) in the eastern and central parts of the basin and positive anomalies (deeper thermocline) in the western Pacific with maxima centered off the equator at

10° – 15°N and $\sim 10^{\circ}\text{S}$. SLP differences reveal high pressure centers in both the Northern and Southern Hemispheres, which are conducive to a strengthening of the easterly trade winds in the tropical Pacific. The Northern Hemisphere SLP anomalies are indicative of a weakened Aleutian low, whereas in the Southern Hemisphere they project on the Pacific–South American pattern (PSA; e.g., Okumura 2013). These differences are very similar, at least qualitatively, to the trends computed by England et al. (2014) over the 1992–2012 period. The differences between P3 and P2, on the other hand, show enhanced anomalies in the Northern Hemisphere relative to the Southern Hemisphere, an equatorial asymmetry possibly associated with the predominance of the NPGO during P3. Indeed, SLP anomalies in the Northern Hemisphere are more similar to the NPO dipole pattern (considered to be

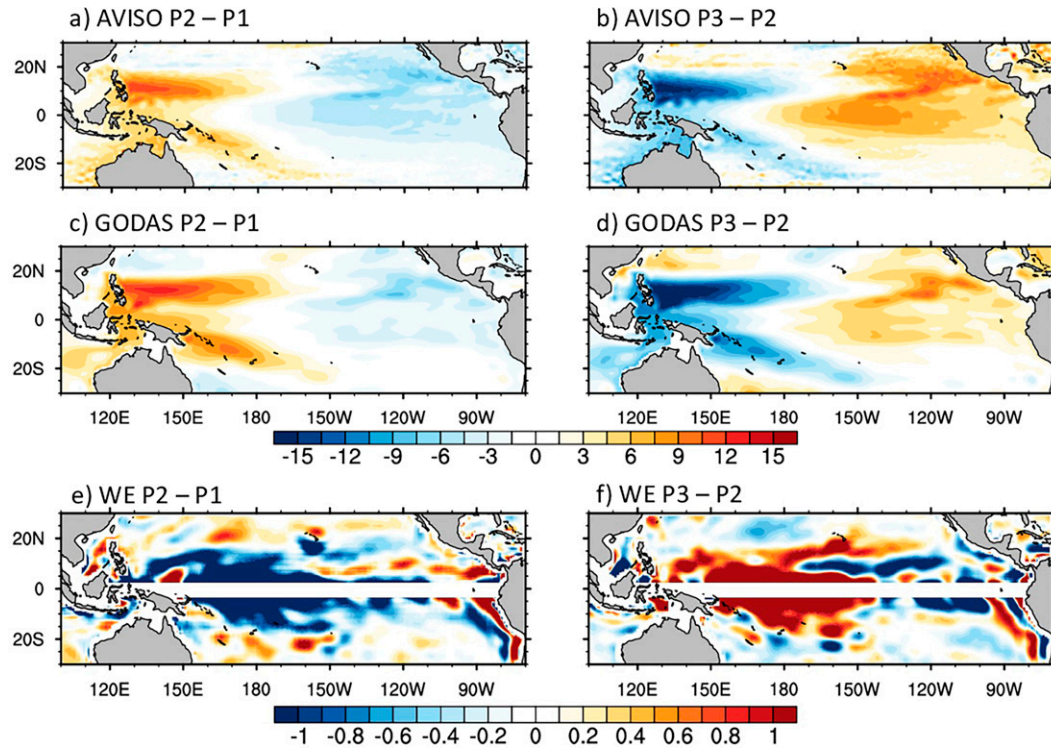


FIG. 3. Epoch differences of SSH (cm) from (a),(b) AVISO and (c),(d) GODAS for (left) P2 minus P1 and (right) P3 minus P2. Also shown are the differences in Ekman pumping (10^{-6} m s^{-1}) $W_E = \nabla \times [\tau/(\rho_0 f)]$ (e) between P2 and P1 and (f) between P3 and P2. All data are detrended over the period 1993–2020 used for the analysis.

the forcing for the NPGO), whose southern negative lobe extends to the northern subtropics, resulting in a pronounced reduction of the Northern Hemisphere off-equatorial trade winds, and intense positive SST anomalies in that subtropical region reminiscent of the North Pacific meridional mode (Chiang and Vimont 2004). The SSH differences during the second transition are roughly of the opposite sign relative to those associated with the first transition, but the presence of a global mean positive SSH trend in the AVISO SSH anomalies (Church and White 2006) results in relative weaker SSH changes between P2 and P3.

In the tropical Pacific, GODAS reproduces the SST epoch changes very closely (not shown), although this is not surprising since the model is relaxed to weekly analyses of observed SSTs. However, GODAS also reproduces the SSH differences reasonably well, even though the altimeter data are not assimilated (Fig. 3). Epoch differences of the anomalous Ekman pumping W_E (Figs. 3e,f) indicate predominantly downwelling conditions during P2 relative to P1 (negative W_E) and upwelling conditions during P3 relative to P2 (positive W_E). The signs of W_E are consistent with the SSH (and thermocline depth) epoch differences in the western Pacific seen in Figs. 3a–d, as expected from wind forced Rossby waves propagation (Merrifield 2011; Qiu and Chen 2012; Yamanaka et al. 2015), and as further discussed in section 5.

Given the connection between SSH and upper-ocean heat content, the good agreement between GODAS and AVISO

provides some confidence that GODAS is suitable for examining subsurface decadal changes. England et al. (2014) showed that during 1992–2012 surface colder conditions were associated with enhanced subsurface heat content. Using a similar approach, we compute epoch differences of meridional temperature sections, and consider their zonal averages in the western and eastern parts of the basin (Fig. 4). Consistent with England et al. (2014), we find that the decadal surface cooling during P2 is mainly confined in the upper 100 meters in the eastern part of the basin, while warm anomalies are mainly seen below 100 m west of the date line. The opposite conditions are seen during P3 relative to P2. We notice that the largest subsurface anomalies are more prominent north of the equator and are located in the main thermocline, as identified by the 15° and 20°C isotherms, suggesting that the origin of these subsurface anomalies may be associated with meridional and vertical thermocline displacements. The enhanced magnitude of the anomalies around 10°N relative to 10°S can be explained with the larger meridional and vertical mean temperature gradients in the Northern Hemisphere, due to the presence of the North Equatorial Countercurrent (NECC).

The time evolution of these subsurface anomalies in the eastern and western parts of the basin, displayed as a function of latitude and time over the full 1980–2020 period covered by GODAS (Fig. 5) reveals a strong ENSO signal in the alternation of positive and negative subsurface temperature anomalies superimposed on a decadal background modulation. Cold and warm background conditions prevail during 1993 to 1999

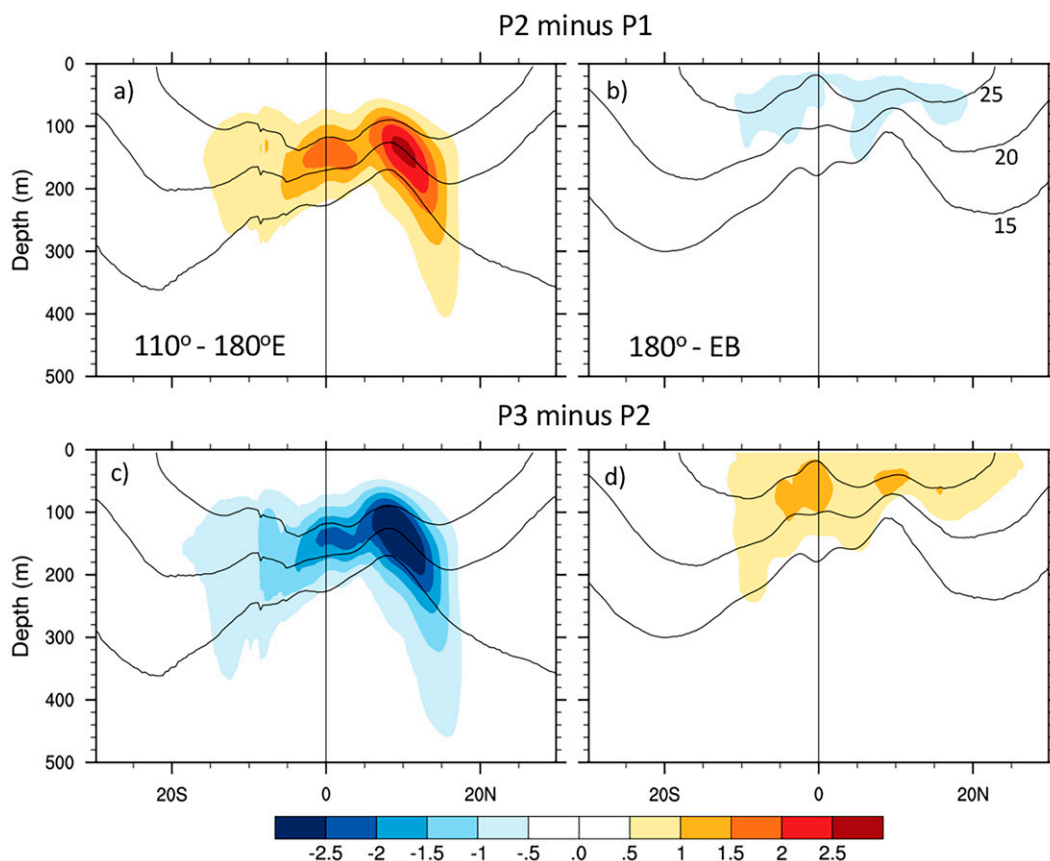


FIG. 4. Epoch differences of subsurface temperature anomalies ($^{\circ}\text{C}$) over the (left) western (110°E – 180°) and (right) eastern (from 180° to the eastern boundary) parts of the tropical Pacific, displayed as a function of latitude (x axis) and depth (y axis), showing (a),(b) P2 minus P1 and (c),(d) P3 minus P2 differences. Contours in each panel show the 15° , 20° , and 25°C climatological isotherms, which span the main thermocline. Note how the anomalies in the western part of the basin occur in the main thermocline.

(i.e., P1) and 2014–20 (i.e., P3) in respectively the western and eastern basins, with opposite conditions during 1999–2014 (a period encompassing P2), as highlighted by the contours of decadal temperature anomalies in Fig. 5. This low-frequency evolution is more pronounced around and poleward of 10° of latitude in both hemispheres, but with larger magnitudes in the Northern Hemisphere.

4. Variability of equatorward interior thermocline transport

The above analysis suggests a profound reorganization of the tropical Pacific upper-ocean heat content during decadal phase transitions. Did the STCs' strength change during these transitions? As shown in previous observational and modeling studies, a useful metric to assess the STC strength is the interior thermocline transport, namely the meridional transport below the surface Ekman layer, and east of the western boundary currents. Following McPhaden and Zhang (2002), previous studies have focused on the transports at 9°N and 9°S , and their convergence. The latitude of 9°N was chosen as

the choke point of the flow in the presence of the potential vorticity barrier created by the northern intertropical convergence zone (ITCZ), while 9°S was chosen for equatorial symmetry. In line with this approach, we have chosen the model's latitudes of 9.5°N and 9.5°S for our transport calculation. Mean sections of the meridional velocities, averaged over the whole 1980–2020 period (Fig. 6) and displayed at longitudes east of the low-latitude western boundary currents (LLWBCs) in both hemispheres, show a clear separation between the poleward flow in the surface Ekman layer (approximately the upper 50 m) and the interior equatorward flow underneath. The largest interior flow is relatively shallow with maxima located around 80 m at both 9.5°N and 9.5°S . We also notice that the transport at 9.5°N is primarily confined west of approximately 160°W , due to the presence of the potential vorticity barrier farther east, while at 9.5°S the equatorward flow extends over a broader range of longitudes, with the largest values seen east of $\sim 145^{\circ}\text{W}$.

Meridional velocity anomalies were computed by first removing the annual cycle over the 1980–2020 period, prior to linearly detrending the data. The anomalous interior transports

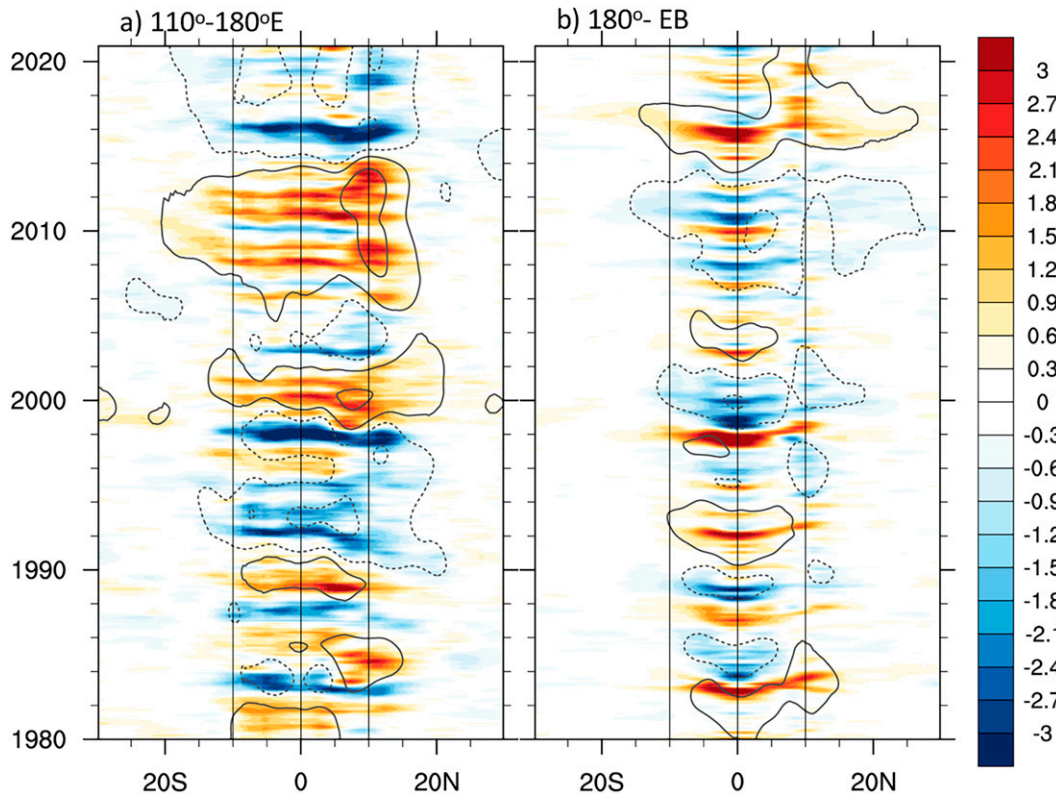


FIG. 5. Latitude–time evolution of subsurface temperature anomalies ($^{\circ}\text{C}$) in the (a) western (110°E – 180°) and (b) eastern (from 180° to the eastern boundary) parts of the basin. Shading shows interannual temperature anomalies, and contours indicate the 0.3° and 1.3°C 6-yr low-pass filtered isotherms, with negative values dashed. Anomalies are integrated between 100 and 200 m in (a) and from the surface to 100 m in (b) to capture the largest anomalies in the two parts of the basin seen in Fig. 4.

were then obtained by integrating the meridional velocity anomalies between 50 and 300 m, and from longitudes just east of the LLWBCs (160°E at 9.5°S and 140°E at 9.5°N) to the eastern ocean boundaries at both latitudes.

The resulting transport time series at 9.5°N and 9.5°S (Figs. 7a,b) show large interannual variations, highlighting the recharge/discharge processes of individual ENSO events. For example, poleward flow is evident at both latitudes during the two extreme El Niño events of 1982/83 and 1997/98, while during the extreme 2015/16 and the weaker 2018/19 El Niño events, discharge occurred primarily in the Northern Hemisphere. These interannual variations of the transports undergo a low-frequency (“decadal”) modulation, as revealed by the 6-yr low-pass filtered time series (purple line), which is obtained through successive applications of centered 25- and 37-month running means, following the approach of Zhang et al. (1997).

Transport convergence across 9.5°S and 9.5°N is computed as the transport at 9.5°S minus the transport at 9.5°N (Fig. 7c). Comparison with SST anomalies averaged over the equatorial Pacific (9.5°S – 9.5°N , 180° – 90°W ; red line) shows a very good correspondence between the two time series (instantaneous correlation coefficient is -0.82), supporting the view that increased thermocline convergence results in enhanced equatorial

upwelling and colder SSTs, while transport divergence leads to decreased upwelling and warmer SSTs. The convergence–SST relationship holds at both interannual (Fig. 7c) and decadal (Fig. 7d) time scales, with a correlation of -0.90 between decadal transport convergence and SST anomalies (Fig. 7d). The relatively high correlation between transport convergence and SST anomalies at interannual time scales was also noted by Schott et al. (2008) and CADM, and can be explained in terms of the recharge or discharge of upper-ocean warm water volume associated with ENSO, as described by the recharge oscillator paradigm (Jin 1997). The transport–SST relationship at decadal time scales suggests that a similar paradigm may also hold at these lower frequencies, as supported by the idealized experiments of Wang et al. (2003). The evolution of the time series at decadal time scales (Fig. 7d) shows that P1 and P3 were characterized by a net divergence (typical of El Niño–like conditions), while P2 was characterized by a net convergence (typical of a La Niña–like decadal state). The changes in interior transport convergence are as large as 10 Sv ($1\text{ Sv} \equiv 10^6\text{ m}^3\text{ s}^{-1}$) between P1 and P2, and about 9.5 Sv between P2 and P3, consistent with estimates of decadal interior transport convergence changes reported in McPhaden and Zhang (2004) and Zhang and McPhaden (2006). The associated SST changes are about 0.5° – 0.6°C .

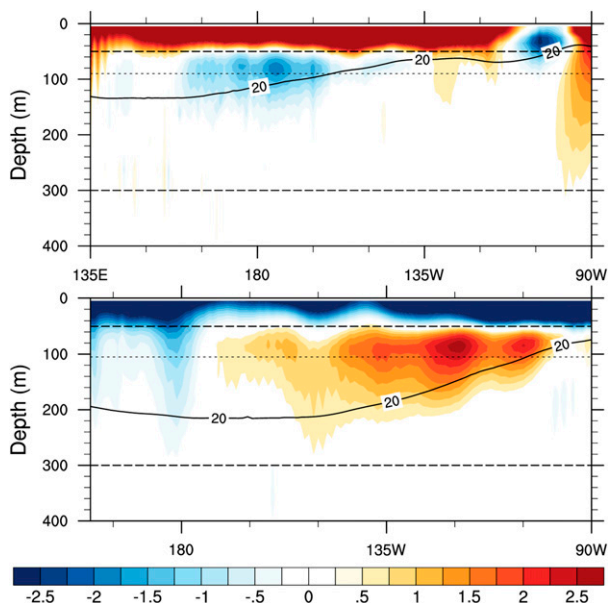


FIG. 6. Sections of mean meridional velocities (cm s^{-1}) at (top) 9.5°N and (bottom) 9.5°S . The mean 20°C isotherm is also shown for reference. Horizontal dashed lines indicate the 50- and 300-m depths that are used for the vertical integration of the interior subsurface transport. Thin horizontal dotted lines show the upper-layer depths chosen for the calculation of the geostrophic transport anomalies at each latitude.

5. How important is the local Ekman pumping in forcing the interior thermocline transport?

While the interior STC transport provides a zonally averaged view of the decadal STC variations, the subsurface changes described in section 3 highlight a more complex three-dimensional structure, with redistribution of subsurface heat content between the eastern and western equatorial Pacific. These subsurface changes are established as the result of an adjustment process that is mediated by oceanic Rossby wave propagation (CADM). Indeed, CADM suggested that the transport changes themselves are established as a result of the passage of westward propagating Rossby waves, and associated anomalies of zonal thermocline slope.

In this section we revisit CADM's suggestion using a 1.5-layer reduced gravity model. Such a model has been shown to be very skillful in reproducing tropical Pacific variability, such as, for example, the variability in the bifurcation latitude of the North Equatorial Current (NEC; Qiu and Chen 2010). Within this framework, the anomalous meridional geostrophic velocity V_g averaged over the upper layer of thickness H can be related to the zonal gradient of the SSH anomalies η as

$$V_g = \frac{gH}{f} \frac{\partial \eta}{\partial x}, \quad (1)$$

where g is the acceleration of gravity, f is the Coriolis parameter, and x is longitude. The zonally integrated geostrophic transport anomaly can be obtained from Eq. (1) as

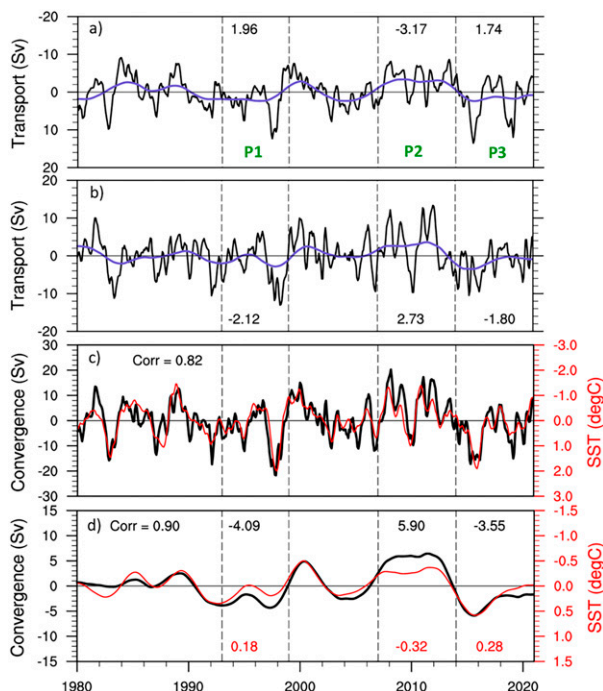


FIG. 7. Time series of equatorward thermocline transport anomalies at (a) 9.5°N and (b) 9.5°S . The vertical axis in (a) is inverted. Vertical dashed lines identify the three periods considered. Numerals at the top of (a) and bottom of (b) indicate the averaged transports at 9.5°N and 9.5°S , respectively, during the three periods. (c) The evolution of the transport convergence (transport at 9.5°S minus the transport at 9.5°N ; black line and left axis) and the evolution of the SST anomalies averaged over the region 9.5°S – 9.5°N , 180° – 270°E (red line and right axis). (d) As in (c), but for 6-yr low-pass filtered transport convergence and SST anomalies. Maximum correlations between SST and transport convergence at interannual and decadal time scales are achieved at lag 0 and are 0.82 (statistically significant above the 99% level) and 0.90 (significant at the 96% level), respectively. Statistical significance of the correlations has been computed using a two-tailed Student's t test, with an effective number of degrees of freedom estimated as in Bretherton et al. (1999) for the time series in (c) and assuming 5 degrees of freedom (corresponding to approximately five 8-yr epochs in the 40-yr GODAS record) for the low-pass filtered time series in (d). Red numerals in (d) indicate the mean values of the low-pass filtered SST anomalies during the three periods. Positive values of the convergence in (c) and (d) indicate enhanced equatorward flow. Note that the SST axis in (c) and (d) is inverted to facilitate the comparison between transport convergence and SST anomalies.

$$\text{Tr}_{\text{SSH}} = \int_{x_1}^{x_2} V_g dx = \frac{gH}{f} [\eta(x_2) - \eta(x_1)], \quad (2)$$

showing that the interior STC transport anomaly between longitudes x_1 and x_2 can be simply expressed in terms of the SSH anomaly difference between those longitudes. The total (vs. anomalous) geostrophic transport also includes an equatorward component in the surface Ekman layer, as shown for the Atlantic Ocean STCs (Tuchen et al. 2019).

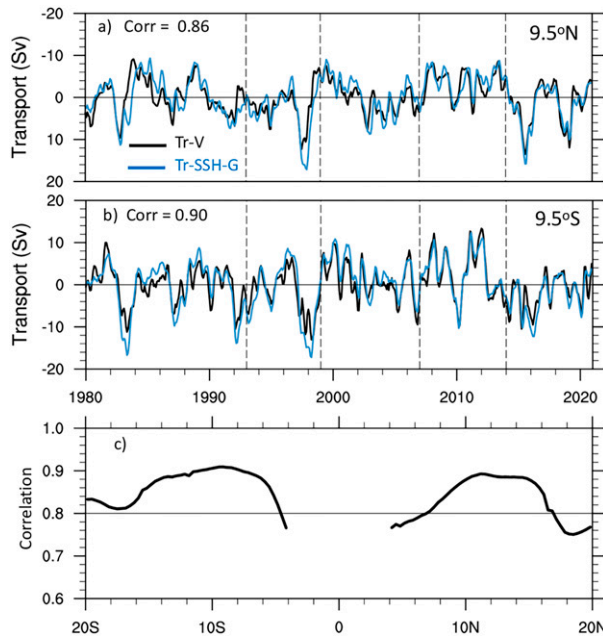


FIG. 8. Comparison between transport anomaly time series estimated from the GODAS meridional velocities (label Tr_V ; black line; as in Fig. 7) and those inferred from the zonal gradient of SSH from GODAS (label $\text{Tr}_{\text{SSH-G}}$; blue line) at (a) 9.5°N and (b) 9.5°S . Correlation coefficients between the two transport estimates are 0.86 at 9.5°N and 0.90 at 9.5°S . See the text for details on the calculation of $\text{Tr}_{\text{SSH-G}}$. (c) Correlation coefficients between Tr_V and $\text{Tr}_{\text{SSH-G}}$, zonally integrated between 180° and 260°E in the Southern Hemisphere and between 140° and 250°E in the Northern Hemisphere, over the 20°S – 20°N latitude range, with the exclusion of the 4°S – 4°N equatorial band. All correlations are statistically significant above the 99% confidence level. The thin black line in (c) highlights the 0.8 correlation coefficient for reference.

We test Eq. (2) by comparing the transport anomaly obtained as the vertical and zonal integral of the GODAS meridional velocity (Tr_V) with the transport anomaly inferred from Eq. (2) using the GODAS SSH anomalies ($\text{Tr}_{\text{SSH-G}}$). The comparison is shown in Figs. 8a and 8b for the transports at 9.5°N and 9.5°S , respectively, where the values of x_1 and x_2 are the same as those used in Fig. 7 ($x_1 = 160^\circ\text{E}$ at 9.5°S and 140°E at 9.5°N and the values of x_2 correspond to the eastern boundary longitudes at each latitude; i.e., 270°E at 9.5°N and 280°E at 9.5°S). The upper-layer depths are chosen as 90 m at 9.5°N , and 105 m at 9.5°S . These depths lie just below the climatological meridional velocity maximum at each latitude, as seen in Fig. 6. The value chosen at 9.5°N coincides with the zonally averaged depth of the 20°C isotherm along that latitude, while the value chosen at 9.5°S is shallower than the zonally averaged depth of the 20°C isotherm (~ 160 m), since at 9.5°S this isotherm deepens significantly in the western part of the basin where the mean meridional flow is small.

Correlation coefficients between Tr_V and $\text{Tr}_{\text{SSH-G}}$ are 0.86 at 9.5°N and 0.90 at 9.5°S , indicating an excellent agreement between the two transport estimates. Both values are statistically significant above the 99% confidence level, based on a

two-sided Student's t test and using an effective number of degrees of freedom calculated according to Bretherton et al. (1999). The relationship between velocity-based and SSH-based meridional transport anomalies, which was never previously demonstrated quantitatively, suggests the possibility of using SSH altimeter data to effectively monitor the STC variability.

To examine whether the relationship between Tr_V and $\text{Tr}_{\text{SSH-G}}$ holds at other tropical latitudes, we compute correlations between the two transport estimates from 20°S to 20°N with the exclusion of the 4°S – 4°N band. For this comparison, we choose the longitudinal limits of integration x_1 and x_2 as 180° – 260°E in the Southern Hemisphere, and 140° – 250°E in the Northern Hemisphere. This choice was made to have the same longitudinal range for all the latitudes considered in each hemisphere, encompassing an area east of the western boundary current and west of the eastern ocean boundary. Results (Fig. 8c) show correlations between Tr_V and $\text{Tr}_{\text{SSH-G}}$ in excess of 0.80 over most of the tropical domain considered, with values as large as 0.91 near 10°S and 0.89 near 11° – 12°N , supporting the hypothesis that a large fraction of the zonally integrated thermocline transport east of the LLWBCs results from anomalous meridional velocities associated with the local zonal gradients of SSH anomalies. The question that then arises is whether these SSH disturbances are due to the passage of westward propagating oceanic Rossby waves forced by the anomalous Ekman pumping along that latitude.

To address this question, we use the 1.5-layer reduced-gravity model:

$$\frac{\partial \eta_m}{\partial t} - c_R \frac{\partial \eta_m}{\partial x} = -\frac{g'}{g} W_E - \epsilon \eta_m, \quad (3)$$

where η_m is SSH anomaly as represented by the model, $c_R(x, y)$ is the Rossby wave phase speed, which varies as a function of latitude y and longitude x , g is the acceleration of gravity, g' is the reduced gravity, ϵ is a Newtonian dissipation rate, and W_E is the Ekman pumping, defined as the curl of the wind stress τ divided by the Coriolis parameter f and by the mean seawater density $\rho_0 = 1025 \text{ kg m}^{-3}$: $W_E = \nabla \times [\tau/(\rho_0 f)]$.

The solution η_m of our reduced gravity model was computed at 9.5°S and 9.5°N by integrating Eq. (3) from the eastern boundary x_e to point x , using the Ekman pumping derived from the wind stress forcing of the GODAS reanalysis:

$$\begin{aligned} \eta_m(x, y, t) = & \frac{g'}{g} \int_{x_e}^x \frac{1}{c_R} W_E \left(x', y, t - \frac{x' - x}{c_R} \right) \exp \left[-\frac{\epsilon}{c_R} (x' - x) \right] dx' \\ & + \int_{x_e}^x \eta_e \exp \left[-\frac{\epsilon}{c_R} (x' - x_e) \right] dx'. \end{aligned} \quad (4)$$

For the chosen latitude y , the solution at each point x and time t arises from two contributions, as indicated by the two terms on the RHS of Eq. (4): the first term is the sum of the signals forced by the Ekman pumping at each longitude x' east of x at times $t - (x' - x)/c_R$, with an e -folding time $1/\epsilon$, while the second term is the contribution of the SSH disturbance at the eastern boundary (η_e), which also decays with an e -folding time $1/\epsilon$ as it propagates westward. We used $g' = 0.07 \text{ m s}^{-2}$ and $\epsilon = (1/2 \text{ yr})^{-1}$. These values were chosen empirically to optimize the comparison between the

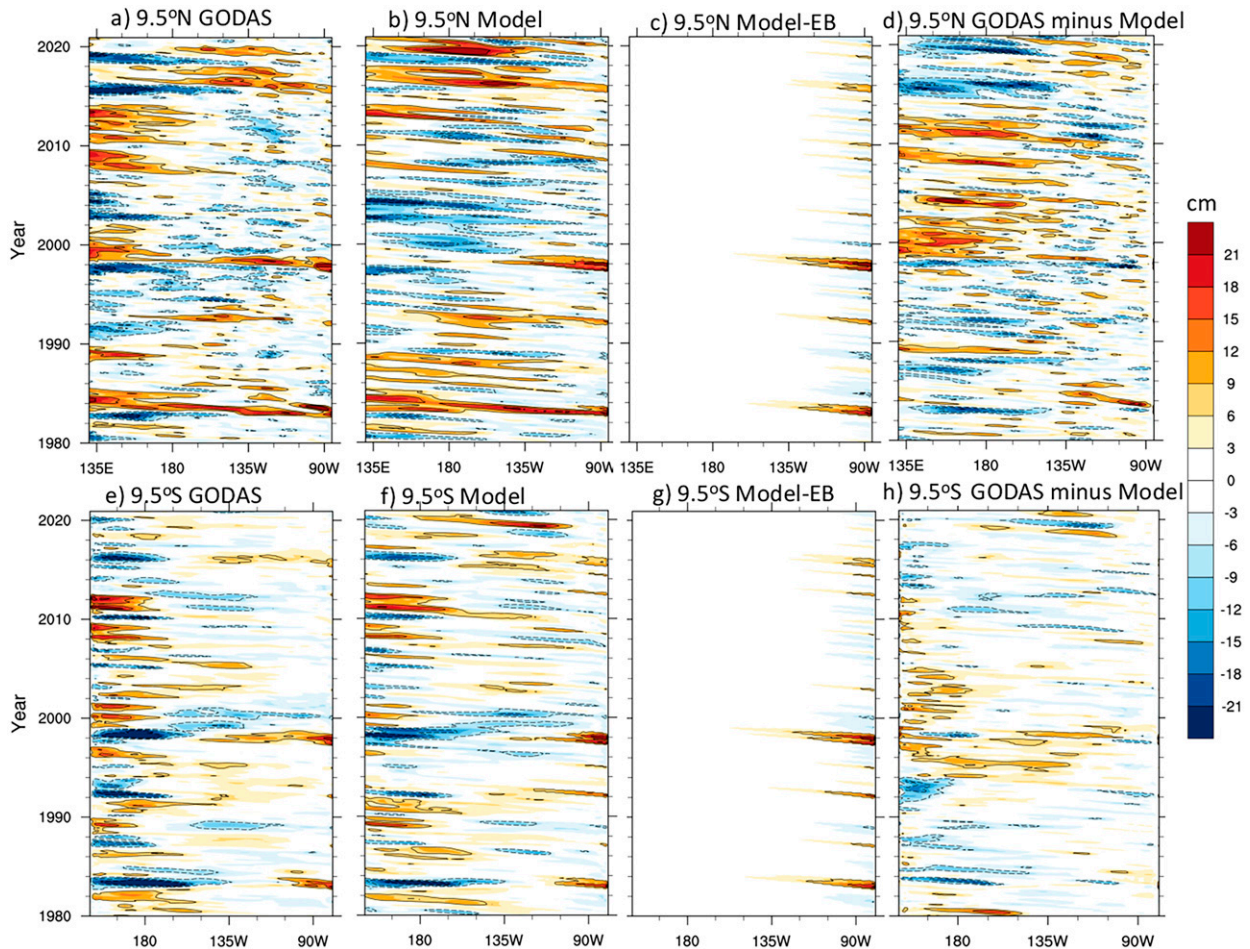


FIG. 9. Evolution of SSH (cm) as a function of longitude (x axis) and time (y axis; time increasing upward) at (top) 9.5°N and (bottom) 9.5°S for (a),(e) GODAS; (b),(f) the reduced gravity model, incorporating both the boundary and wind-forced components; and (c),(g) the reduced gravity model boundary-forced component only. Also shown are (d) the difference between (a) and (b) and (h) the difference between (e) and (f). Contours are plotted at intervals of 7 cm, with negative values dashed. The pattern correlation between (a) and (b) is 0.58, and the pattern correlation between (e) and (f) is 0.74.

modeled SSH anomalies and those obtained from the GODAS output. Finally, the spatially dependent values of c_R were determined from the GODAS density fields using the Wentzel–Kramers–Brillouin approximation, following the approach outlined in Chelton et al. (1998). The values of c_R increase from approximately $20\text{--}22\text{ cm s}^{-1}$ at the eastern boundary to $\sim 30\text{--}32\text{ cm s}^{-1}$ in the western part of the basin at both latitudes, in relatively good agreement with the observationally derived estimates (Chelton et al. 1998). The solution in Eq. (4) relies on the assumption that Rossby waves propagate westward along latitude circles, which is a good approximation at the time scales we are interested in (Schopf et al. 1981).

The longitude–time evolutions of the SSH anomalies obtained by integrating Eq. (4) at 9.5°N and 9.5°S are compared with the evolution of the GODAS anomalies in Fig. 9. At 9.5°N the pattern correlation between the GODAS and modeled anomalies (Figs. 9a,b) is 0.58. While the overall evolution is captured by the model, several features are either underestimated or overestimated, especially in the western part of the

domain and after the year 2000, as highlighted by their difference (Fig. 9d). Figure 9d shows, in particular, the model underestimation of the positive SSH anomalies in the western Pacific associated with the La Niña events of 1998–2001, 2007–09, and 2010–12, as well as the weaker model representation of the negative anomalies related to the El Niño events of 2015/16 and 2018/19. As a result, the decadal “envelope” of these events is underestimated with overall weaker positive SSH anomalies in 2000–14 and weaker negative anomalies during 2014–20. While these discrepancies could be partly attributed to the simplicity of the model, it is also possible that a fraction of SSH variations at this latitude may be contributed by wind variations at some higher latitude, as suggested in previous studies (Farneti et al. 2014). Given the presence of the potential vorticity barrier around $7^{\circ}\text{--}12^{\circ}\text{N}$ (McPhaden and Zhang 2002), a fraction of the meridional transports originating north of the barrier could be deflected southwestward and contribute to the SSH variations at 9.5°N . The potential influence of wind variations at higher latitudes,

and the dependence of their influence on the specific characteristics of the wind variability warrant further investigation in future studies. A better agreement between the SSH anomalies from GODAS and the reduced gravity model is found at 9.5°S (Figs. 9e,f,h), and quantitatively confirmed by the value of the pattern correlation (0.74), and by the smaller differences seen in Fig. 9h.

The third column in Fig. 9 shows the contribution of the SSH disturbances at the eastern boundary. While large signals are seen within $\sim 30^\circ$ from the eastern boundary in conjunction with the 1982/83 and 1997/98 events, the contribution of the eastern boundary anomalies is generally small even in the case of the extreme El Niño of 2015/16. This event had its largest anomalies displaced farther west than the 1982/83 and 1997/98 events (Capotondi et al. 2020a), resulting in weaker SSH anomalies in the eastern equatorial Pacific and correspondingly weaker coastally trapped waves along the western coast of the Americas.

The interior transport anomalies inferred from Eq. (2) at 9.5°N and 9.5°S, using the values of η_m calculated from the 1.5-layer reduced-gravity model (referred to as $\text{Tr}_{\text{SSH-M}}$) are compared with Tr_V in Fig. 10. Correlation coefficients between the two transport estimates are 0.77 at 9.5°N and 0.84 at 9.5°S, statistically significant above the 99% confidence level based on a two-sided Student's t test. Although these correlation coefficients are slightly lower than those obtained from the SSH anomalies from GODAS, they still account for about 60% and 70% of the transport variance at 9.5°N and 9.5°S, respectively. Thus, we conclude that a large fraction of the interior thermocline transport variations is established as a result of the westward propagation of oceanic Rossby waves forced by the local Ekman pumping and is in balance with the zonal gradient of SSH anomalies resulting from that adjustment process.

6. Discussion

The $v'\bar{T}$ mechanism, as originally formulated, hypothesized that wind variability in extratropical regions could change the strength of the subtropical cells, and alter equatorial SSTs through changes in equatorial upwelling. Our results confirm that interior transport convergence is strongly related to changes in equatorial SSTs. However, those transport changes appear to be primarily controlled by *local* Ekman pumping variations at the same latitude, rather than by *remote* wind variations. At decadal time scales, however, some influences from higher latitudes cannot be ruled out especially at 9.5°N and after the year 2000, consistent with previous studies (e.g., Klinger et al. 2002; Nonaka et al. 2002; Farneti et al. 2014; Graffino et al. 2019). Further investigations are needed to clarify this point.

We also show that the establishment of the transport changes through oceanic Rossby wave propagation connects variability in the interior equatorward flow with the zonal changes in SSH and upper-ocean heat content. While the importance of wind-driven Rossby wave activity for tropical SSH variations is not new (e.g., Qiu and Chen 2010; Yamanaka et al. 2015; Ishizaki et al. 2019), here we more specifically and quantitatively relate that concept to STC transport changes.

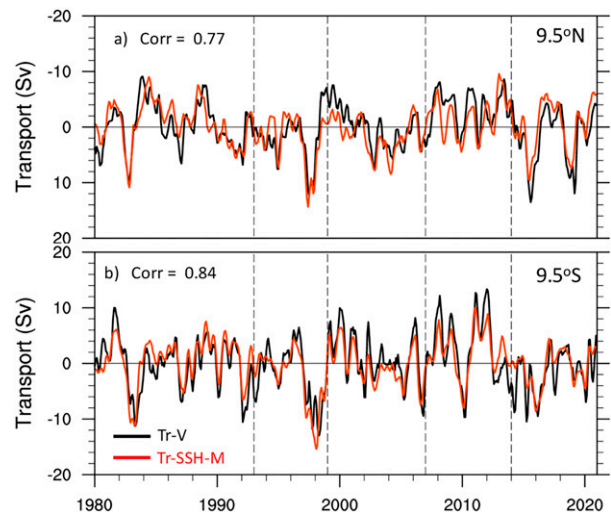


FIG. 10. Comparison between transport anomaly time series estimated from the GODAS meridional velocities (label Tr_V ; black line; as in Figs. 7 and 8) and those inferred from the zonal gradient of SSH from the reduced-gravity model (label $\text{Tr}_{\text{SSH-M}}$; red line) at (a) 9.5°N and (b) 9.5°S. Correlation coefficients between the two transport estimates are 0.77 at 9.5°N and 0.84 at 9.5°S. Correlations are statistically significant above the 99% confidence level, based on a two-sided Student's t test.

This study has focused on the interior equatorward transport of the STCs east of the low-latitude western boundary currents. Previous modeling studies, primarily conducted with models of relatively coarse horizontal resolution (Lee and Fukumori 2003; CADM), have indicated a partial compensation between the interior and boundary current transport anomalies, a result supported by observational studies (Zilberman et al. 2013), which could potentially reduce the STCs' influence on equatorial upwelling and SSTs. In this study we have shown the ability of a 1.5-layer reduced-gravity model to capture the adjustment of the equatorial thermocline to Ekman pumping variations, in agreement with previous studies (e.g., Qiu and Chen 2010, 2012). This adjustment results in the decadal SSH changes seen in Fig. 3. By geostrophy, the positive SSH anomalies seen in the western Pacific during P2 relative to P1 (Figs. 3a,c) would imply clockwise (anticlockwise) circulations in the Northern (Southern) Hemisphere, with anomalous poleward boundary current flow during a phase of predominantly equatorward anomalous interior flow. The opposite can be expected in P3 relative to P2, thus explaining the partial compensation of the boundary and interior transports. This interpretation is consistent with the argument presented by McPhaden and Zhang (2004), based on Sverdrup theory. These results suggest that the boundary current changes may be largely confined to the tropical gyre circulation in the western Pacific, and not significantly influence the equatorial thermocline in the central-eastern Pacific, but additional research is needed to further elucidate this point. Given the complexity of the LLWBCs, additional observations are also needed to constrain these features in ocean and climate models, and better understand their role in equatorial Pacific variability.

Some studies have hypothesized that tropical Pacific decadal variability may arise as a residual of ENSO events (Vimont 2005; Rodgers et al. 2004; Power et al. 2021). Differences in the evolution of individual ENSO events, from the precursor phase to the mature and decay phases, may result in decadal averages with a spatial pattern similar to the decadal SST pattern. Asymmetries in amplitude and spatial pattern between the El Niño and La Niña phases of ENSO can also be expected to contribute to El Niño-like or La Niña-like decadal epochs with a larger number of El Niño or La Niña events, respectively (Power et al. 2021). Possible dynamical nonlinearities may also lead to the rectification of ENSO characteristics into the mean state (Rodgers et al. 2004). The results presented in this paper show, indeed, that ENSO variations dominate the evolution of interior transports. However, our results also indicate that decadal changes in the tropical Pacific thermocline depth and circulation result primarily from wind variability. Thus, if TPDV simply arises as an ENSO residual, this must happen through the ENSO influence on the tropical winds.

One important open question concerns the origin of the tropical wind anomalies associated with decadal variations. We can speculate that if the wind response to ENSO-related SST anomalies occasionally extends poleward, this could lengthen the adjustment process of the equatorial thermocline to time scales in the decadal range due to the decrease of the Rossby wave phase speed with increasing latitude. Wind variations associated with internal modes of extratropical atmospheric variability, such as the North Pacific Oscillation (NPO; Rogers 1981) and the South Pacific Oscillation (SPO; You and Furtado 2017) have been associated with important ENSO precursors, especially for central Pacific (CP) event types (Capotondi and Ricciardulli 2021). The SST signatures of these precursors are known as the Pacific meridional mode (PMM; Chiang and Vimont 2004) and the South Pacific meridional mode (SPMM; Zhang et al. 2014). Paleoclimate records show that the PMM exhibits enhanced decadal variability (Sanchez et al. 2016), suggesting the possibility that the associated winds may also contain a decadal component that could force tropical decadal variations. Modeling studies indicate that Atlantic SST anomalies could modulate the Pacific tropical winds at decadal time scales, although the magnitude of this influence appears to be model dependent (Ruprich-Robert et al. 2021). Future studies need to identify the characteristics of the tropical wind forcing that are critical for promoting and sustaining decadal variations. In particular, it would be very important to understand whether TPDV is simply associated with the reddening of stochastic atmospheric forcing, which may be white in frequency domain, (e.g., Zhao and Di Lorenzo 2020) through the ocean thermodynamic (Hasselmann 1976) or dynamic (Capotondi et al. 2003) integration of that forcing, or whether it can be viewed as a coupled cyclic phenomenon that involves a wind response to decadal SST anomalies.

7. Conclusions

In this study, we have examined the changes in the tropical surface and subsurface fields that have occurred during

1980–2020 across decadal epochs associated with warmer and cooler surface conditions in the equatorial Pacific. One of these epochs is the recent 2014–20 period, whose characteristics relative to previous periods had not yet been documented. Our results indicate a return to warmer than average SSTs after 2014, following the colder than average conditions during 2000–13. Tropical winds appear to play a key role in shaping the equatorial Pacific at decadal time scales. Decadal epochs characterized by stronger trade winds are associated with enhanced heat content in the western Pacific thermocline and depleted heat content in the upper ocean of the central and eastern parts of the basin. Conversely, decadal epochs characterized by weaker trade winds are associated with reduced heat content in the western Pacific thermocline and enhanced heat content in the upper ocean of the central and eastern parts of the basin. While such changes were previously noted in conjunction with the cooling trend that occurred during the first decade of the twenty-first century (e.g., England et al. 2014), here we more explicitly relate these changes at each latitude to Ekman pumping variations along that same latitude, and to the oceanic adjustment through oceanic Rossby wave propagation. Weaker trade winds correspond to prevailing positive Ekman pumping anomalies, which force upwelling Rossby waves, and result in a shallower thermocline in the western tropical Pacific, corresponding to reduced heat content in that area. Conversely, stronger trade winds correspond to prevailing negative Ekman pumping anomalies, which force downwelling Rossby waves, and result in a deeper thermocline in the western tropical Pacific, corresponding to enhanced heat content in that area. This zonal reorganization of heat content supports, in turn, changes in the zonally integrated interior equatorward transport, which can modulate equatorial upwelling affecting SST (and mixed-layer temperature) in the central/eastern part of the basin.

The results presented here are based on one ocean reanalysis. Similar diagnostics should be extended to other ocean reanalyses to assess their robustness across products that differ in their choice of ocean model, assimilation method and surface forcing.

Given the key role played by climate models for providing future projections, it is very important that decadal variability is simulated realistically by those models to properly isolate climate change signals from internal variability. Indeed, studies have indicated a muted expression of tropical Pacific decadal variability in climate models (e.g., Parsons et al. 2017), and the inability of many climate models to reproduce the observed relationship between interior transport convergence and equatorial SST anomalies (Zhang and McPhaden 2006; Graffino et al. 2021). Also, while the pattern of Pacific decadal variability may appear “realistic” in the current generation of climate models (e.g., Capotondi et al. 2020b), no systematic analyses of the models have been conducted to assess whether those patterns are associated with the correct underlying oceanic processes. Diagnostic approaches similar to those described in this study can provide a suitable avenue for assessing model fidelity from a dynamical viewpoint. In particular, the relationship identified in this study between the geostrophic transport, as determined through the zonal SSH gradient, and the actual meridional transport could be used as a dynamical metric for

evaluating model performance. Such analyses will be undertaken in future work.

Acknowledgments. Author Capotondi was supported by the NOAA Climate Program Office Climate Variability and Predictability (CVP) Program. Author Qiu was supported by the Physical Oceanography Program of NASA (80NSSC21K0552, 80NSSC21K1186). The authors thank three anonymous reviewers for their excellent and constructive comments, which have greatly improved the paper.

Data availability statement. The monthly data of the GODAS output were obtained from the NOAA Physical Sciences Laboratory (<https://www.esrl.noaa.gov/psd/data/gridded/data.godas.html>). The same website was also used to obtain the NOAA OISST (<https://www.psl.noaa.gov/data/gridded/data.noaa.oisst.v2.html>) and the SLP and surface wind data (<https://psl.noaa.gov/data/gridded/data.ncep.reanalysis.surface.html>). AVISO data were also obtained online (<http://www.aviso.oceanobs.com/en/data/products/>).

REFERENCES

- Augustine, J. A., and A. Capotondi, 2022: Forcing for multidecadal surface solar radiation trends over Northern Hemisphere continents. *J. Geophys. Res. Atmos.*, **127**, e2021JD036342, <https://doi.org/10.1029/2021JD036342>.
- Behringer, D. W., and Y. Xue, 2004: Evaluation of the global ocean data assimilation system at NCEP: The Pacific Ocean. *Eighth Symp. on Integrated Observing and Assimilation Systems for Atmosphere, Oceans, and Land Surface*, Seattle, WA, Amer. Meteor. Soc., 2.3, https://ams.confex.com/ams/84Annual/techprogram/paper_70720.htm.
- Bond, N. A., J. E. Overland, M. Spillane, and P. Stabeno, 2003: Recent shifts in the state of the North Pacific. *Geophys. Res. Lett.*, **30**, 2183, <https://doi.org/10.1029/2003GL018597>.
- Bretherton, C. S., M. Widmann, V. P. Dymnikov, J. M. Wallace, and I. Bladé, 1999: The effective number of spatial degrees of freedom of a time-varying field. *J. Climate*, **12**, 1990–2009, [https://doi.org/10.1175/1520-0442\(1999\)012<1990:TENOSD>2.0.CO;2](https://doi.org/10.1175/1520-0442(1999)012<1990:TENOSD>2.0.CO;2).
- Capotondi, A., and M. A. Alexander, 2001: Rossby waves in the tropical North Pacific and their role in decadal thermocline variability. *J. Phys. Oceanogr.*, **31**, 3496–3515, [https://doi.org/10.1175/1520-0485\(2002\)031<3496:RWITTN>2.0.CO;2](https://doi.org/10.1175/1520-0485(2002)031<3496:RWITTN>2.0.CO;2).
- , and L. Ricciardulli, 2021: The influence of Pacific winds on ENSO diversity. *Sci. Rep.*, **11**, 18672, <https://doi.org/10.1038/s41598-021-97963-4>.
- , M. A. Alexander, and C. Deser, 2003: Why are there Rossby wave maxima in the Pacific at 10°S and 13°N? *J. Phys. Oceanogr.*, **33**, 1549–1563, <https://doi.org/10.1175/2407.1>.
- , —, and M. J. McPhaden, 2005: Anatomy and decadal evolution of the Pacific subtropical–tropical cells (STCs). *J. Climate*, **18**, 3739–3758, <https://doi.org/10.1175/JCLI3496.1>.
- , and Coauthors, 2015: Understanding ENSO diversity. *Bull. Amer. Meteor. Soc.*, **96**, 921–938, <https://doi.org/10.1175/BAMS-D-13-00117.1>.
- , A. T. Wittenberg, J.-S. Kug, K. Takahashi, and M. J. McPhaden, 2020a: ENSO diversity. *El Niño Southern Oscillation in a Changing Climate*, A. Santoso, W. Cai, and M. McPhaden, Eds., Amer. Geophys. Union, 65–86, <https://doi.org/10.1002/9781119548164.ch4>.
- , C. Deser, A. S. Phillips, Y. Okumura, and S. M. Larson, 2020b: ENSO and Pacific decadal variability in the Community Earth System Model version 2. *J. Adv. Model. Earth Syst.*, **12**, e2019MS002022, <https://doi.org/10.1029/2019MS002022>.
- , M. Newman, T. Xu, and E. Di Lorenzo, 2022: An optimal precursor of northeast Pacific marine heatwaves and central Pacific El Niño events. *Geophys. Res. Lett.*, **49**, e2021GL097350, <https://doi.org/10.1029/2021GL097350>.
- Chavez, F. P., J. Ryan, S. E. Lluch-Cota, and C. Miguel Niquen, 2003: From anchovies to sardines and back: Multidecadal change in the Pacific Ocean. *Science*, **299**, 217–221, <https://doi.org/10.1126/science.1075880>.
- Chelton, D. B., R. A. de Szoeke, M. G. Schlax, K. E. Naggar, and N. Siwertz, 1998: Geographical variability of the first baroclinic Rossby radius of deformation. *J. Phys. Oceanogr.*, **28**, 433–460, [https://doi.org/10.1175/1520-0485\(1998\)028<0433:GVOTFB>2.0.CO;2](https://doi.org/10.1175/1520-0485(1998)028<0433:GVOTFB>2.0.CO;2).
- Cheng, W., M. J. McPhaden, D. Zhang, and E. Metzger, 2007: Recent changes in the Pacific subtropical cells inferred from an eddy-resolving ocean circulation model. *J. Phys. Oceanogr.*, **37**, 1340–1356, <https://doi.org/10.1175/JPO3051.1>.
- Chiang, J. C. H., and D. J. Vimont, 2004: Analogous Pacific and Atlantic meridional modes of tropical atmosphere–ocean variability. *J. Climate*, **17**, 4143–4158, <https://doi.org/10.1175/JCLI4953.1>.
- Church, J. A., and N. J. White, 2006: A 20th century acceleration in global sea-level rise. *Geophys. Res. Lett.*, **33**, L01602, <https://doi.org/10.1029/2005GL024826>.
- Di Lorenzo, E., and Coauthors, 2008: North Pacific gyre oscillation links ocean climate and ecosystem change. *Geophys. Res. Lett.*, **35**, L08607, <https://doi.org/10.1029/2007GL032838>.
- , and Coauthors, 2022: Modes and mechanisms of Pacific decadal-scale variability. *Annu. Rev. Mar. Sci.*, <https://doi.org/10.1146/annurev-marine-040422-084555>, in press.
- England, M. H., and Coauthors, 2014: Recent intensification of wind-driven circulation in the Pacific and the ongoing warming hiatus. *Nat. Climate Change*, **4**, 222–227, <https://doi.org/10.1038/nclimate2106>.
- Farneti, R., S. Dwivedi, F. Kucharski, F. Molteni, and S. M. Griffies, 2014: On Pacific subtropical cell variability over the second half of the twentieth century. *J. Climate*, **27**, 7102–7112, <https://doi.org/10.1175/JCLI-D-13-00707.1>.
- Graffino, G., R. Farneti, F. Kucharski, and F. Molteni, 2019: The effect of wind stress anomalies and location in driving Pacific subtropical cells and tropical climate. *J. Climate*, **32**, 1641–1660, <https://doi.org/10.1175/JCLI-D-18-0071.1>.
- , —, and —, 2021: Low-frequency variability of the Pacific subtropical cells as reproduced by coupled models and ocean reanalyses. *Climate Dyn.*, **56**, 3231–3254, <https://doi.org/10.1007/s00382-021-05639-6>.
- Gu, D., and S. G. H. Philander, 1997: Interdecadal climate fluctuations that depend on exchange between the tropics and extratropics. *Science*, **275**, 805–807, <https://doi.org/10.1126/science.275.5301.805>.
- Hasselmann, K., 1976: Stochastic climate models, Part I: Theory. *Tellus*, **28A**, 473–485, <https://doi.org/10.3402/tellusa.v28i6.11316>.
- Henley, B. J., J. Gergis, D. J. Karoly, S. Power, J. Kennedy, and C. K. Folland, 2015: A tripole index for the interdecadal

- Pacific oscillation. *Climate Dyn.*, **45**, 3077–3090, <https://doi.org/10.1007/s00382-015-2525-1>.
- Huang, B., and Coauthors, 2017: Extended Reconstructed Sea Surface Temperature, version 5 (ERSSTv5): Upgrades, validations and intercomparisons. *J. Climate*, **30**, 8179–8205, <https://doi.org/10.1175/JCLI-D-16-0836.1>.
- Imada, Y., H. Tatebe, M. Watanabe, M. Ishii, and M. Kimoto, 2016: South Pacific influence on the termination of El Niño in 2014. *Sci. Rep.*, **6**, 30341, <https://doi.org/10.1038/srep30341>.
- Ishizaki, H., T. Nakano, H. Nakano, and G. Yamanaka, 2019: Interdecadal variability of the North Equatorial Undercurrent (NEUC) found in the long-term hydrographic observations along 137°E. *J. Oceanogr.*, **75**, 395–414, <https://doi.org/10.1007/s10872-019-00509-6>.
- Jin, F.-F., 1997: An equatorial ocean recharge paradigm for ENSO. Part I: Conceptual model. *J. Atmos. Sci.*, **54**, 811–829, [https://doi.org/10.1175/1520-0469\(1997\)054<0811:AEORPF>2.0.CO;2](https://doi.org/10.1175/1520-0469(1997)054<0811:AEORPF>2.0.CO;2).
- Kalnay, E., and Coauthors, 1996: The NCEP/NCAR 40-Year Reanalysis Project. *Bull. Amer. Meteor. Soc.*, **77**, 437–472, [https://doi.org/10.1175/1520-0477\(1996\)077<0437:TNYRP>2.0.CO;2](https://doi.org/10.1175/1520-0477(1996)077<0437:TNYRP>2.0.CO;2).
- Kleeman, R., J. P. McCreary Jr., and B. A. Klinger, 1999: A mechanism for generating ENSO decadal variability. *Geophys. Res. Lett.*, **26**, 1743–1746, <https://doi.org/10.1029/1999GL900352>.
- Klinger, B., J. P. McCreary Jr., and R. Kleeman, 2002: The relationship between oscillating subtropical wind stress and equatorial temperature. *J. Phys. Oceanogr.*, **32**, 1507–1521, [https://doi.org/10.1175/1520-0485\(2002\)032<1507:TRBOSW>2.0.CO;2](https://doi.org/10.1175/1520-0485(2002)032<1507:TRBOSW>2.0.CO;2).
- Kosaka, Y., and S.-P. Xie, 2013: Recent global warming hiatus tied to equatorial Pacific surface cooling. *Nature*, **501**, 403–407, <https://doi.org/10.1038/nature12534>.
- Lee, T., and I. Fukumori, 2003: Interannual-to-decadal variations of tropical-subtropical exchange in the Pacific Ocean: Boundary vs. interior pycnocline transports. *J. Climate*, **16**, 4022–4042, [https://doi.org/10.1175/1520-0442\(2003\)016<4022:IVOTEI>2.0.CO;2](https://doi.org/10.1175/1520-0442(2003)016<4022:IVOTEI>2.0.CO;2).
- Lübbecke, J. F., C. W. Böning, and A. Biastoch, 2008: Variability in the subtropical–tropical cells and its effect on near-surface temperature of the equatorial Pacific: A model study. *Ocean Sci.*, **4**, 73–88, <https://doi.org/10.5194/os-4-73-2008>.
- Mantua, N. J., S. R. Hare, Y. Zhang, J. M. Wallace, and R. C. Francis, 1997: A Pacific interdecadal climate oscillation with impacts on salmon production. *Bull. Amer. Meteor. Soc.*, **78**, 1069–1080, [https://doi.org/10.1175/1520-0477\(1997\)078<1069:APICOW>2.0.CO;2](https://doi.org/10.1175/1520-0477(1997)078<1069:APICOW>2.0.CO;2).
- McCreary, J. P., Jr., and P. Lu, 1994: Interaction between the subtropical and the equatorial oceans: The subtropical cell. *J. Phys. Oceanogr.*, **24**, 466–497, [https://doi.org/10.1175/1520-0485\(1994\)024<0466:IBTSAE>2.0.CO;2](https://doi.org/10.1175/1520-0485(1994)024<0466:IBTSAE>2.0.CO;2).
- McPhaden, M. J., and D. Zhang, 2002: Slowdown of the meridional overturning circulation in the upper Pacific Ocean. *Nature*, **415**, 603–608, <https://doi.org/10.1038/415603a>.
- , and —, 2004: Pacific Ocean circulation rebounds. *Geophys. Res. Lett.*, **31**, L18301, <https://doi.org/10.1029/2004GL020727>.
- Meehl, G. A., A. Hu, and H. Teng, 2016: Initialized decadal prediction for transition to positive phase of the interdecadal Pacific oscillation. *Nat. Commun.*, **7**, 11718, <https://doi.org/10.1038/ncomms11718>.
- , H. Teng, A. Capotondi, and A. Hu, 2021: The role of interannual ENSO events in decadal timescale transitions of the interdecadal Pacific Oscillation. *Climate Dyn.*, **57**, 1933–1951, <https://doi.org/10.1007/s00382-021-05784-y>.
- Merrifield, M. A., 2011: A shift in western tropical Pacific sea level trends during the 1990s. *J. Climate*, **24**, 4126–4138, <https://doi.org/10.1175/2011JCLI3932.1>.
- Newman, M., and Coauthors, 2016: The Pacific decadal oscillation, revisited. *J. Climate*, **29**, 4399–4427, <https://doi.org/10.1175/JCLI-D-15-0508.1>.
- Nonaka, M., S.-P. Xie, and J. P. McCreary, 2002: Decadal variations in the subtropical cells and equatorial Pacific SST. *Geophys. Res. Lett.*, **29**, 1116, <https://doi.org/10.1029/2001GL013717>.
- Okumura, Y. M., 2013: Origins of tropical Pacific decadal variability: Role of stochastic atmospheric forcing from the South Pacific. *J. Climate*, **26**, 9791–9796, <https://doi.org/10.1175/JCLI-D-13-00448.1>.
- Parsons, L. A., G. R. Loope, J. T. Overpeck, T. R. Ault, R. Syouffer, and J. E. Cole, 2017: Temperature and precipitation variance in CMIP5 simulations and paleoclimate records of the last millennium. *J. Climate*, **30**, 8885–8912, <https://doi.org/10.1175/JCLI-D-16-0863.1>.
- Power, S., and Coauthors, 2021: Decadal climate variability in the tropical Pacific: Characteristics, causes, predictability and prospects. *Science*, **374**, eaay9165, <https://doi.org/10.1126/science.aay9165>.
- Qiu, B., and S. Chen, 2010: Interannual-to-decadal variability in the bifurcation of the North Equatorial Current off the Philippines. *J. Phys. Oceanogr.*, **40**, 2525–2538, <https://doi.org/10.1175/2010JPO4462.1>.
- , and —, 2012: Multidecadal sea level and gyre circulation variability in the northwestern tropical Pacific Ocean. *J. Phys. Oceanogr.*, **42**, 193–206, <https://doi.org/10.1175/JPO-D-11-061.1>.
- Reynolds, R. W., N. A. Rayner, T. M. Smith, D. C. Stokes, and W. Wang, 2002: An improved in situ and satellite SST analysis for climate. *J. Climate*, **15**, 1609–1625, [https://doi.org/10.1175/1520-0442\(2002\)015<1609:AIISAS>2.0.CO;2](https://doi.org/10.1175/1520-0442(2002)015<1609:AIISAS>2.0.CO;2).
- Rodgers, K. B., P. Friederichs, and M. Latif, 2004: Tropical Pacific decadal variability and its relation to decadal modulations of ENSO. *J. Climate*, **17**, 3761–3774, [https://doi.org/10.1175/1520-0442\(2004\)017<3761:TPDVAI>2.0.CO;2](https://doi.org/10.1175/1520-0442(2004)017<3761:TPDVAI>2.0.CO;2).
- Rogers, J. C., 1981: The North Pacific oscillation. *J. Climatol.*, **1**, 39–57, <https://doi.org/10.1002/joc.3370010106>.
- Ruprich-Robert, Y., and Coauthors, 2021: Impacts of Atlantic multidecadal variability on the tropical Pacific: A multi-model study. *npj Climate. Atmos. Sci.*, **4**, 33, <https://doi.org/10.1038/s41612-021-00188-5>.
- Sanchez, S. C., C. D. Charles, J. D. Carriquiry, and J. A. Villaseca, 2016: Two centuries of coherent decadal climate variability across the Pacific North America region. *Geophys. Res. Lett.*, **43**, 9208–9216, <https://doi.org/10.1002/2016GL069037>.
- Schneider, N., A. J. Miller, M. A. Alexander, and C. Deser, 1999: Subduction of decadal North Pacific temperature anomalies: Observations and dynamics. *J. Phys. Oceanogr.*, **29**, 1056–1070, [https://doi.org/10.1175/1520-0485\(1999\)029<1056:SODNPT>2.0.CO;2](https://doi.org/10.1175/1520-0485(1999)029<1056:SODNPT>2.0.CO;2).
- Schopf, P. S., D. L. T. Anderson, and R. Smith, 1981: Beta-dispersion of low-frequency Rossby waves. *Dyn. Atmos. Oceans*, **5**, 187–214, [https://doi.org/10.1016/0377-0265\(81\)90011-7](https://doi.org/10.1016/0377-0265(81)90011-7).
- Schott, F. A., W. Wang, and D. Stammer, 2007: Variability of Pacific subtropical cells in the 50-year ECCO assimilation. *Geophys. Res. Lett.*, **34**, L05604, <https://doi.org/10.1029/2006GL028478>.
- , L. Stramma, W. Wang, B. S. Giese, and R. Zantopp, 2008: Pacific subtropical cell variability in the SODA 2.0/23

- assimilation. *Geophys. Res. Lett.*, **35**, L10607, <https://doi.org/10.1029/2008GL033757>.
- Solomon, A., J. P. McCreary Jr., R. Kleeman, and B. A. Klinger, 2003: Interannual and decadal variability in an intermediate coupled model of the Pacific region. *J. Climate*, **16**, 383–405, [https://doi.org/10.1175/1520-0442\(2003\)016<0383:IADVIA>2.0.CO;2](https://doi.org/10.1175/1520-0442(2003)016<0383:IADVIA>2.0.CO;2).
- Trenberth, K. E., and J. W. Hurrell, 1994: Decadal atmosphere–ocean variations in the Pacific. *Climate Dyn.*, **9**, 303–319, <https://doi.org/10.1007/BF00204745>.
- Tuchen, F. P., J. F. Lübbecke, S. Schmidtke, R. Hummels, and C. W. Böning, 2019: The Atlantic subtropical cells inferred from observations. *J. Geophys. Res. Oceans*, **124**, 7591–7605, <https://doi.org/10.1029/2019JC015396>.
- Vimont, D. J., 2005: The contribution of the interannual ENSO cycle to the spatial pattern of decadal ENSO-like variability. *J. Climate*, **18**, 2080–2092, <https://doi.org/10.1175/JCLI3365.1>.
- Wang, X., F.-F. Jin, and Y. Wang, 2003: A tropical ocean recharge mechanism for climate variability: Part II: A unified theory of decadal and ENSO modes. *J. Climate*, **16**, 3599–3616, [https://doi.org/10.1175/1520-0442\(2003\)016<3599:ATORMF>2.0.CO;2](https://doi.org/10.1175/1520-0442(2003)016<3599:ATORMF>2.0.CO;2).
- Wei, W., Z. Yan, and Z. Li, 2021: Influence of Pacific decadal oscillation on global precipitation extremes. *Environ. Res. Lett.*, **16**, 044031, <https://doi.org/10.1088/1748-9326/abed7c>.
- Yamanaka, G., H. Tsujino, H. Nakano, and M. Hirabara, 2015: Decadal variability of the Pacific subtropical cells and its relevance to the sea surface height in the western tropical Pacific during recent decades. *J. Geophys. Res. Oceans*, **120**, 201–224, <https://doi.org/10.1002/2014JC010190>.
- You, Y., and J. C. Furtado, 2017: The role of South Pacific atmospheric variability in the development of different types of ENSO. *Geophys. Res. Lett.*, **44**, 7438–7446, <https://doi.org/10.1002/2017GL073475>.
- Zeller, M., S. McGregor, E. van Sebille, A. Capotondi, and P. Spence, 2021: Subtropical-tropical pathways of spiciness anomalies and their impact on equatorial Pacific temperatures. *Climate Dyn.*, **56**, 1131–1144, <https://doi.org/10.1007/s00382-020-05524-8>.
- Zhang, D., and M. J. McPhaden, 2006: Decadal variability of the shallow Pacific meridional overturning circulation: Relation to tropical sea surface temperatures in observations and climate change models. *Ocean Modell.*, **15**, 250–273, <https://doi.org/10.1016/j.ocemod.2005.12.005>.
- Zhang, H., A. Clement, and P. P. Di Nezio, 2014: The South Pacific meridional mode: A mechanism for ENSO-like variability. *J. Climate*, **27**, 769–783, <https://doi.org/10.1175/JCLI-D-13-00082.1>.
- Zhang, Y., J. M. Wallace, and D. S. Battisti, 1997: ENSO-like interdecadal variability: 1900–93. *J. Climate*, **10**, 1004–1020, [https://doi.org/10.1175/1520-0442\(1997\)010<1004:ELIV>2.0.CO;2](https://doi.org/10.1175/1520-0442(1997)010<1004:ELIV>2.0.CO;2).
- Zhao, Y., and E. Di Lorenzo, 2020: The impacts of extra-tropical ENSO precursors on tropical Pacific decadal-scale variability. *Sci. Rep.*, **10**, 3031, <https://doi.org/10.1038/s41598-020-59253-3>.
- Zilberman, N. V., D. H. Roemmich, and S. T. Gille, 2013: The mean and the time variability of the shallow meridional overturning circulation in the tropical South Pacific Ocean. *J. Climate*, **26**, 4069–4087, <https://doi.org/10.1175/JCLI-D-12-00120.1>.